Journal of
Materials Chemistry C

PAPER

Cite this: DOI: 10.1039/d5tc01514f

Dual functionality of phosphorescence and photothermal conversion through light-activated open-shell singlet diradicals in silver metal–organic frameworks†

Pei-Yu Liao,‡ Jia-Chuan Liu,‡ Hao-Zhi Fan, Yi Ding and Ming-Liang Tong *

Received 12th April 2025,
Accepted 2nd July 2025

DOI: 10.1039/d5tc01514f

rsc.li/materials-c

Synergistically regulating the photoluminescence properties and photothermal conversion performance is a highly concerning and challenging task, and constructing radical-induced photochromic materials is one of the effective strategies. In this work, we exploited the structural advantages of crystalline MOF materials, assembled using the photoactive TEPE ligands and the silver ions, and further introduced the large steric ADC$^-$ (ADCA = 1-adamantane carboxylic acid) guests to form [Ag(TEPE)](ADC)·9H_2O (**1**). MOF **1** rapidly forms photochromic product **1*** under 365 nm light irradiation, and time-dependent EPR characterization verifies that the photoinduced radicals maintained good stability against water and oxygen. Interestingly, the variable-temperature EPR spectrum exhibits a rare thermal enhancement phenomenon, which is a typical characteristic of thermally excited triplet diradicals. Steady-state photoluminescence spectra showcase the transition from **1** with blue emission to **1*** with red/NIR emission, while transient-state decay spectra account for the lifetimes ranging from nanoseconds to microseconds, confirming the emergence of a thermally excited triplet state. Under a 0.5 W 808 nm laser, the photothermal conversion efficiency of **1*** is 49.05%. The remarkable solar-driven water evaporation efficiency is 80% under Xenon lamp irradiation, and the average water evaporation amount is 1.232 kg m^{-2} h^{-1}. The photoinduced thermally excited triplet radicals not only activate the room-temperature phosphorescence behavior but also trigger the outstanding photothermal conversion performance, and triple responses of magnetic/optical/thermal effects can be further realized.

Introduction

A diradical refers to a system possessing two unpaired spins, one of which is known as the thermally excited triplet state, also termed the open-shell singlet state, and has received extensive attention recently.[1–5] At low temperatures, the interacting pair of electrons is in a spin-paired singlet state (S = 0). As temperature increases, the spin-paired diradical transforms into a spin-parallel triplet state (S = 1).[6–9] Currently, thermally excited triplet state materials have been widely utilized in fields such as optical display, spin storage, photoelectric semiconductors, and others.[10–15]

At present, there are two main synthesis strategies for thermally excited triplet materials. Firstly, the components with electron transfer activity (*i.e.*, the electron donors and the acceptors) are assembled together, and the intramolecular electron transfer process is achieved through thermal stimulation at high temperature (*e.g.*, solvothermal method), thereby achieving the characteristics of diradical materials.[16,17] Secondly, unpaired single electrons are obtained through the use of chemical reagents with strong oxidizing and reducing properties in organometallic synthesis.[18–21] However, both of these strategies require energy-intensive and multi-step synthesis, and thus the development of clean, facile, and controllable strategies is highly desirable.[22] Photochromic materials are a class of optical functional materials with color bistability, and can realize a synergistic regulation of physical and chemical properties through remote controlled light irradiation.[23–26] Among them, radical-induced photochromic materials are some of the most promising emerging materials, not only because they can exhibit rapid and significant color changes but also, more importantly, the multifunctional responses of optical, magnetic, and thermal effects can be activated by photoinduced radicals.[27–29] For instance, excellent optical properties such as typical aggregation-induced luminescence effects and room-temperature phosphorescence properties are achieved in

---

Key Laboratory of Bioinorganic and Synthetic Chemistry of Ministry of Education, School of Chemistry, IGCME, GBRCE for Functional Molecular Engineering, Sun Yat-Sen University, Guangzhou 510006, P. R. China.
E-mail: tongml@mail.sysu.edu.cn

† Electronic supplementary information (ESI) available: Photochromic characterization, optical spectra and EPR data, information of crystallography and DFT calculations. CCDC 2415265. For ESI and crystallographic data in CIF or other electronic format see DOI: https://doi.org/10.1039/d5tc01514f

‡ These authors contributed equally to this work.

many cases.[30,31] However, it is extremely difficult to manipulate the spin state of photoinduced radicals in a directional manner, and there is still a lack of design schemes to introduce thermally excited triplet diradicals into radical-induced photochromic materials through synthesis.

Photothermal conversion is another significant application of thermally excited triplet diradical materials. In particular, near-infrared (NIR) thermal conversion materials can efficiently utilize the NIR light region that accounts for a certain proportion of sunlight to achieve the conversion of light energy into heat energy.[32–34] At the same time, when thermally excited triplet materials are used to meet the real-world demand for freshwater enrichment, their performance in both water evaporation and conversion efficiency is not inferior to that of inorganic nanomaterials.[35–39] Herein, we develop a synthesis strategy for introducing thermally excited triplet photoinduced radicals with strong air/water stability into high-performance NIR photothermal conversion materials. By selecting non-conjugated large steric-hindered anionic guests to fill the cavities, the host–guest electronic interactions with the silver ion framework are weakened and the intrinsic properties of the main skeleton are revealed. The spectroscopic properties of stable photoinduced radicals were successfully investigated through EPR characterization, and the transient-state photoluminescence spectra further validated the existence of triplets with a phosphorescence lifetime of approximately 2.5 ms at room temperature. The outstanding solar-driven water evaporation performance broadens the practical application of photochromic materials in photothermal conversion performance, and provides a blueprint for the future directional design and synthesis of high-performance photoluminescence/photothermal conversion materials.

Results and discussion

Compositional and structural characterization

The synthesis of MOF **1** was carried out by means of a mild solution approach. In a homogeneous solution, $[Ag(NH_3)_2]^+$ ions and four-connected TEPE ligands self-assemble to form an ordered metal–organic framework, while the ordered cavity filled with large-scale anionic ADC$^-$ guests forms the target product **1** (Fig. 1a). Thermogravimetric analysis, infrared analysis, and elemental analysis are conducive to disclosing the detailed composition information, indicating that the pores of each individual unit were filled with nine H_2O molecules (Fig. S1 and S2, ESI†). The room temperature powder diffraction pattern of **1** is in excellent accordance with the simulation diagram, which ensures the purities of the samples for the subsequent characterization (Fig. S3, ESI†).

In order to further discuss the interaction between the main framework and guest molecules, we analyze the structural composition of MOF **1** through single-crystal X-ray diffraction (SC-XRD). MOF **1** crystallizes in the orthorhombic *Pcca* space group (Table S1, ESI†), and its asymmetric unit contains an independent silver ion with a distorted tetrahedral local configuration that is coordinated with μ_4-TEPE ligands (Fig. 1b). The average Ag–N bond length is 2.318 Å, and the N–Ag–N bond angles range from 84.84° to 118.55° (Table S2, ESI†), demonstrating the feature of a distorted tetrahedral coordination geometry. As can be seen in the three-dimensional (3D) stacking diagram, **1** possesses exquisitely structured pores and cavities that are ready to accommodate large-sized guest molecules (Fig. 1c and Fig. S4, ESI†). Probing into the characteristics of the pores, the filled ADC$^-$ anions are in a disordered state since the non-conjugated anionic guests do not have sufficient host–guest interactions with the main framework, and thus lack fixed conformations (Fig. 1d). By abstracting the Ag ions and TEPE ligand as four-connected nodes, the topology of **1** can be analyzed using the TOPOSPro software. A classical 4,4-connected **sqc**183 topological framework with point symbol $\{4^2\cdot8^4\}$ is obtained (Fig. 1e).

Interestingly, even though the topology of **1** is very similar to that of the 4-connected structures of the silver-MOFs we have previously published,[28] its linker TEPE is rather distorted. As Fig. 1f shows, the dihedral angles of adjacent pyridine rings are extremely discrepant, ranging from 48.68° to 87.22°. For structures with conjugated anions, however, the four dihedral angles of NC/BC are basically close, indicating that the TEPE ligands do not experience significant rotational distortion (Table S3, ESI†). The ligand distortion effect was also observed in another silver-MOF NTF with a non-conjugated anionic guest. By quantifying the distortion degree of the TEPE linker with variance, it can be clearly seen that ADCA (MOF **1**) > NTF > NC = BC (Fig. 1g). This phenomenon reveals that the main framework of Ag-MOF determines the allowable size of the guests, but the space structures and degrees of conjugation of the anionic guests can dynamically regulate the conformation of the linkers, thereby expressing the property differences driven by the host–guest interaction.

Photochromism and photoinduced radicals

MOF **1** showcases distinct and rapid photochromism under the perturbation of UV light. Under room light conditions, **1** appears as a pale-yellow crystal, but after 365 nm light irradiation, the color deepens significantly and is visibly stabilized to a brownish-red color (Fig. 2a). Time-dependent ultraviolet-visible-near infrared (UV-Vis-NIR) reflection spectra display the photo-responsive behaviors of **1** and the corresponding photoproduct **1***. Before 365 nm light irradiation, the absorption of **1** is only concentrated in the deep UV region, with the central absorption at around 294 nm. After illumination, the absorption characteristics of **1*** change drastically. The original absorption gradually decreases, while the absorption from the near UV to NIR region increases significantly (Fig. 2b). By splitting each characteristic absorption peak of **1*** for more detailed examination, the UV, visible, and NIR regions show different behaviors. With the increase of the three-hour illumination time, the peaks positioned at 276 nm and 294 nm continue to decrease (Fig. 2c). These locations belong to the characteristic absorption of the ethylene bond, suggesting the presence of the photoactive sites of **1**.[40–42] In the visible region, the changes at 470, 512 and 556 nm are mainly investigated. The absorption increases rapidly within 10 minutes of irradiation and remains basically stable after

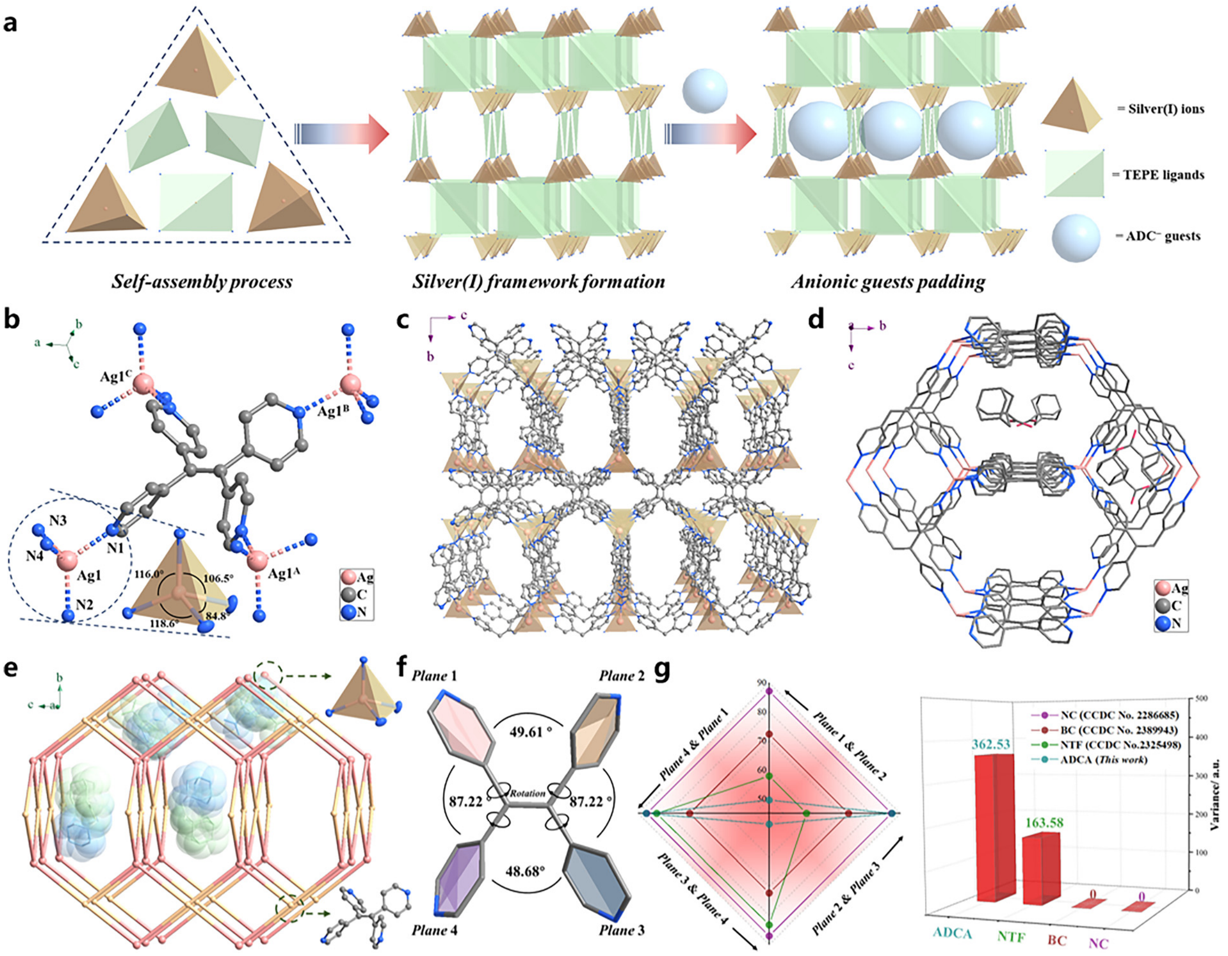

Fig. 1 (a) Synthesis roadmap of the framework-assembly and guest-encapsulation processes for target silver MOF **1**. Therein, the yellow tetrahedron represents the central silver ion, the green deformed polyhedron represents the TEPE ligand, and the blue sphere represents the ADC⁻ guest. (b) Coordination environment of TEPE ligands and silver atoms. The anionic guests are omitted for clarity. Color code: Ag, pink; N, dark blue; and C, grey. Symmetry code: (a) ^{A} −*X*, *Y*, 1/2 − *Z*; ^{B} −1/2 + *X*, 1 − *Y*, 1/2 − *Z*; and ^{C} 1/2 − *X*, 1 − *Y*, *Z*. (c) 3D packing structure along the *a*-axis direction. (d) In order to further exhibit the relative position of the framework and guests, ADC⁻ anionic guests are filled into the pores in the *a*-axis stacking diagram. (e) The topological analysis of **1**. The silver ions and μ_4-TEPE are regarded as 4-connected nodes and linkers, respectively. The selected anionic guests are represented as space-filling mode with green and blue spheres to represent two disordered parts. (f) Diagram of the distortion of TEPE ligands. The colored planes represent the different pyridine ring planes, and the numbers in the figure represent the dihedral angles of the adjacent planes. (g) Dihedral angle data and statistical diagrams of 4-connected silver MOFs with μ_4-TEPE ligand coordination. The ordinate value is the variance of the four dihedral angles of each silver MOF. The five symbols represent different anionic guest names whose crystal structures have been published: NC for the 1-naphthoic anion (CCDC 2286685†), BC for the 1-benzoic anion (CCDC 2389943†), NTF for bis(trifluoromethylsulfonyl)imide (CCDC 2325498†), and ADCA for the 1-amantadanic anion. Color code: NC, pale purple; BC, dark red; NTF, green; and ADCA, aqua green.

20 minutes, indicating the accumulation of ethylene-bond radicals in **1*** (Fig. 2d). More importantly, **1*** acts differently in the NIR region compared to the visible region (Fig. 2e). The increase in its absorption slows down, and even when it reaches a steady state at 3 hours, it still maintains an upward trend. This phenomenon hints at the potentially excellent NIR-photothermal conversion behaviors, and the mechanism will be further analyzed combining with theoretical calculations.

The PXRD pattern of photoirradiation product **1*** displays a slightly higher angular shift compared to MOF **1** before 365 nm light irradiation (Fig. S5, ESI†). In order to further discuss the initiation mechanism of the photothermal reaction, parallel tests were carried out on MOF **1** at different power densities of irradiation light sources. The threshold for the light-driven reaction was 130 mW cm^{-2} (Fig. S6, ESI†). Furthermore, an investigation into the reversibility of **1*** which had been placed in the dark for one week was performed. The slight change in absorbance confirmed that the photophysical properties of light-stable **1*** could be maintained for a long time (Fig. S7, ESI†). According to previous studies, the emergence of ethylene-bond radicals can distort the skeleton of silver MOFs, thus resulting in a slightly higher angular shift in the PXRD pattern.[28,43,44] In order to further verify the above conjecture, we further conducted variable-temperature EPR measurements on **1***. As shown in Fig. 2f, there is an obvious organic radical signal at a *g*-value of 2.005 (at 337 mT), confirming the production of TEPE radicals. Intriguingly, with the increase of temperature, the intensity of EPR does not minish due to the

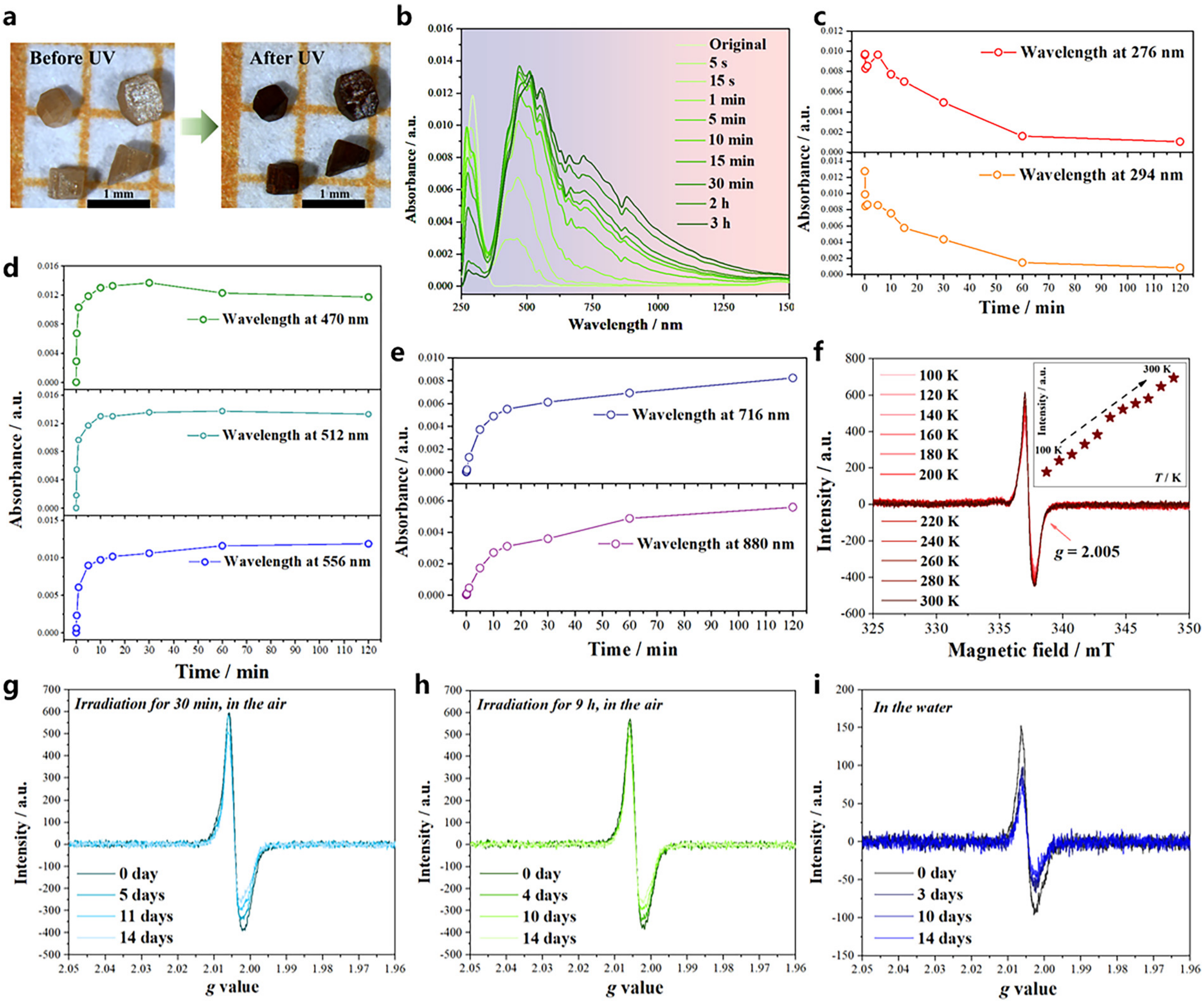

Fig. 2 (a) The photochromic pictures of complexes before (left) and after (right) UV light irradiation. (b) Time-dependent UV-Vis-NIR diffuse reflection spectra of **1** in the solid state after being irradiated with 365 nm light. (c) The changes in absorbance of the absorption peaks of **1** at 276 nm (red) and 294 nm (orange). (d) The changes in absorbance of the absorption peaks of **1** at 470 nm (green), 512 nm (aqua green) and 556 nm (blue). (e) The changes in absorbance of the absorption peaks of **1** at 716 nm (dark purple) and 880 nm (purple). (f) Solid-state temperature-dependent EPR spectra of **1*** from 100 K to 300 K. The inset presents the variation of the EPR intensity with temperature. (g) Solid-state time-dependent EPR spectra of **1*** after the removal of external 365 nm irradiation at room temperature. Sample **1*** was irradiated for 30 minutes in the air. (f) Solid-state time-dependent EPR spectra of **1*** after the removal of external 365 nm irradiation at room temperature. Sample **1*** was irradiated for 9 hours in the air. (i) Solid-state time-dependent EPR spectra of **1***, which was stored by being immersed in water.

common thermal quenching phenomenon, but rather an obvious thermal enhancement performance can be observed (Fig. S8, ESI†).[45–47] In other words, the fundamental reason for breaking the EPR silence of **1** is the existence of the thermally excited triplet state, and it has been proved that a half-field transition signal is hard to be captured either in a powder sample or a solution sample.[48]

In order to assess the stability of the thermal excited triplet state of **1***, time-dependent EPR spectra were obtained for the **1*** sample that was exposed to the air and water. Firstly, EPR tests were performed on **1*** that had been illuminated for 30 minutes, and it was observed that the signal of the sample gradually weakened as time increased. Nevertheless, the radical signal was still detectable after 14 days (Fig. 2g and Fig. S9, ESI†). Additionally, after re-testing the samples that had been exposed to 9 hours of 365 nm light irradiation under the same conditions, we were surprised to find that the relaxation process of its EPR signal was consistent with that of the previous samples (Fig. 2h). The EPR spectra of samples with different irradiation durations within similar time periods were successively compared, and the intensity and location were basically similar. This phenomenon indicates that **1*** has a rapid photoresponse rate, and the generation process of photoinduced radicals can be accomplished within a short time achieving stable performance for a long period. Time-dependent EPR characterization upon water immersion is conducive to exploring the resistance to water erosion of sample **1***. As depicted in Fig. 2i, the EPR intensity changes rapidly in the initial stage of water immersion (within 0–3 days) and then stabilizes at a fixed value. The above studies have shown that the photoinduced radicals in **1*** have a strong ability to resist the destruction by air and water and exhibit ultrahard EPR activities.

Ultralong-decay photoluminescence behavior

The steady-state and transient-state photoluminescence spectra are collected to study the optical characteristics of MOFs **1** and **1***. The excitation spectra monitored at the characteristic emission wavelengths exhibit the broadband nature, indicating that the emissions of **1** and **1*** can be excited at multiple wavelengths (Fig. S10, ESI†). Under the excitation at 355 nm, the emission broad band of **1** at 100 K is concentrated at around 450 nm, and with the increase of temperature, a blue shift occurs at 430 nm and 300 K (Fig. 3a and Fig. S11, ESI†). The lifetime decay curves at 100/160/240/300 K were monitored under the excitation at 405 nm, where the values obtained by double exponential fitting at 100 K are approximately 1 ns

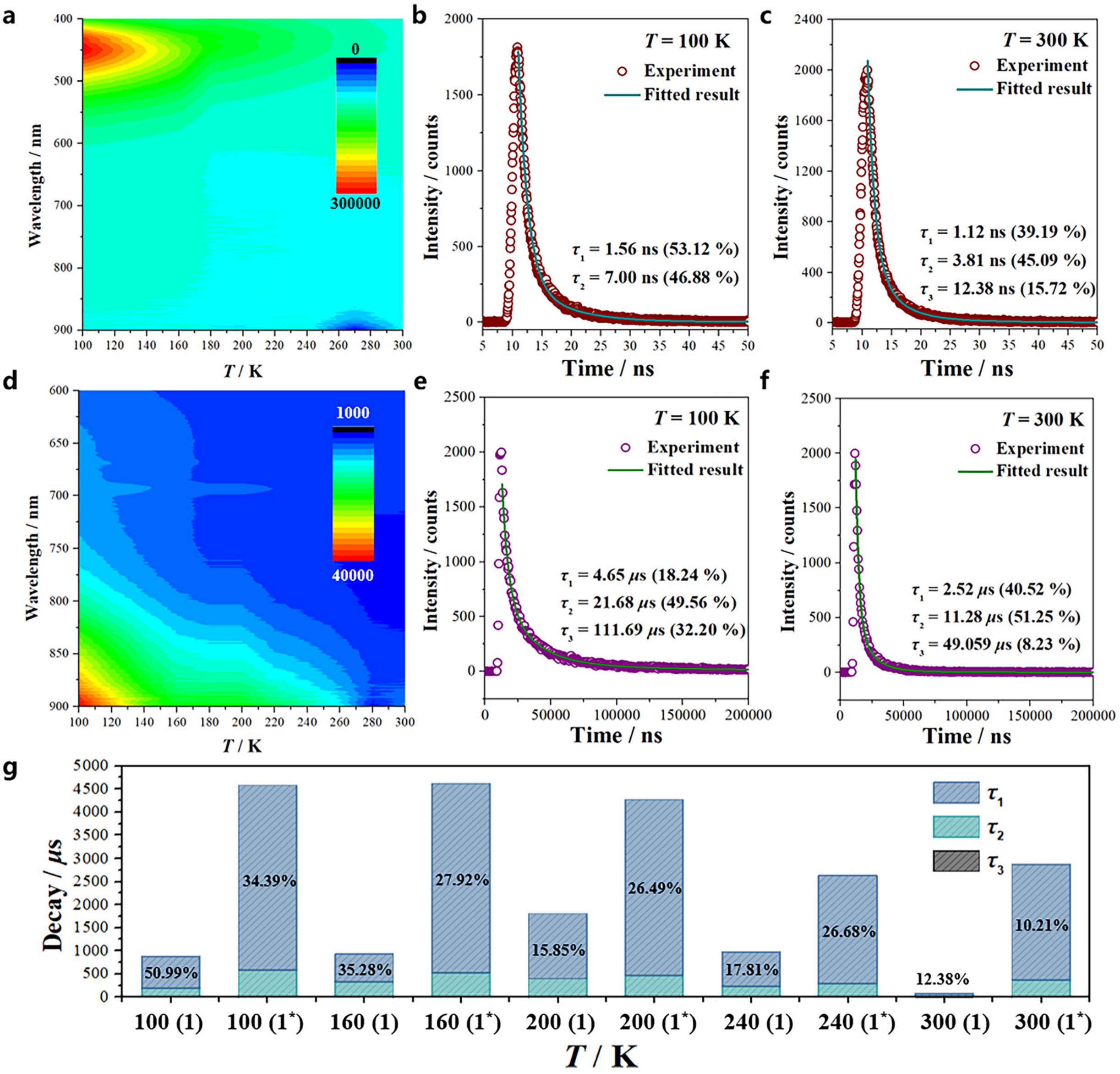

Fig. 3 (a) Temperature-dependent emission spectra of **1** (excited at 355 nm) in the solid state ranging from 100 K to 300 K. (b) Lifetime measurements for **1** in the solid state at 100 K, with the mean lifetime of τ_1 = 1.56 ns (53.12%) and τ_2 = 7.00 ns (46.88%), which are fitted by a double exponential function (λ_{ex} = 405 nm and λ_{em} = 450 nm). (c) Lifetime measurements for **1** in the solid state at 300 K, with the mean lifetime of τ_1 = 1.16 ns (39.19%), τ_2 = 3.81 ns (45.09%) and τ_3 = 12.38 ns (15.72%), which are fitted by a triple exponential function (λ_{ex} = 405 nm and λ_{em} = 450 nm). (d) Temperature-dependent emission spectra of **1*** (excited at 355 nm) in the solid state from 100 K to 300 K. (e) Lifetime measurements for **1*** in the solid state at 100 K, with the mean lifetime of τ_1 = 4.46 μs (18.24%), τ_2 = 21.68 μs (49.56%) and τ_3 = 111.69 μs (32.20%), which are fitted by a triple exponential function (λ_{ex} = 355 nm and λ_{em} = 850 nm). (f) Lifetime measurements for **1** in the solid state at 300 K, with the mean lifetime of τ_1 = 2.52 μs (40.52%), τ_2 = 11.28 μs (51.25%) and τ_3 = 49.06 μs (8.23%), which are fitted by a triple exponential function (λ_{ex} = 355 nm and λ_{em} = 850 nm). (g) Under 355 nm excitation, the decay curves were collected for **1** and **1*** at an emission wavelength of 650 nm, and the statistical graph of the lifetime results obtained by triple-exponential fitting is used, where the numbers represent the proportion of the longest lifetime (τ_1). Color code: τ_1, blue; τ_2, green; and τ_3, black.

and 7 ns (Fig. 3b and Fig. S12, ESI†). At room temperature, a slightly longer lifetime of about 12 ns can be obtained by using three exponential function analysis (Fig. 3c).

Comparatively, the emission behavior of **1*** has changed significantly, covering from 550 nm to 900 nm, and the central position is concentrated at 850 nm, while the NIR photoluminescence is the characteristic performance of organic radicals (Fig. 3d and Fig. S13, ESI†).[49–51] Transient-state decay behavior of **1*** realizes the transition from nanoseconds to microseconds, suggesting the generation of triplet state products.[52,53] The attenuation behavior of **1*** becomes very complicated, and the decay results of the distribution range can be obtained by three-exponential fitting of the lifetime curves for different temperatures (from 100 to 300 K). The basic rule can be summarized as that the absolute value and proportion of long-lived τ_3 gradually decrease with the increase of temperature (Fig. 3e, f and Fig. S14, ESI†). It demonstrates that relaxation of the triple state at low temperatures favors radiative transition mechanisms, while at high temperatures, it favors other relaxation processes, such as the thermal energy conversion processes of non-radiative transitions.

To further explore the impact of photo-induced radicals on the photoluminescence behavior, the crossed emission bands of **1** and **1*** at 650 nm were monitored under 355 nm excitation. The interferon regulatory factor (IRF) excited by a 355 nm microsecond pulse lamp was collected to assess the influence of the background (Fig. S15, ESI†), and the fitted IRF result is 3.9 μs. Thus, we believe that the three fitted sets of lifetimes are from the sample. The decay of MOF **1** at 650 nm is on the order of microseconds, but both the lifetime length and the relative proportion are affected by temperature (Fig. 3g and Fig. S16, S17, ESI†). The summary tables of the decay lifetimes and relative proportions of **1** and **1*** are presented in Tables S4–S6 (ESI†). It can be observed that the phosphorescence decay lifetimes at 650 nm (15385 $\mathrm{cm^{-1}}$) are longer than those at 850 nm (11765 $\mathrm{cm^{-1}}$) at different temperatures. The above results indicate that the energy transfer pathway may be from the singlet state to the high-energy triplet state (650 nm), and then shift to a low-energy triplet state (850 nm), thereby leading to differences in decay lifetimes.

In order to further analyze the blue-light fluorescence emission of MOF **1** at the central position of 450 nm and the red-light and near-infrared phosphorescence emissions of **1*** at 650 and 850 nm,[54–56] the fluorescence intensity ratio (FIR) was utilized to describe the dynamic change of **1***. Given the fluorescence emission behavior at 450 nm of MOF **1**, we take the intensity at 450 nm of **1*** as the reference and evaluate their absolute sensitivities (S_a) and relative sensitivities (S_r). The data were measured using the following equations: FIR = $A \times \exp(-T/B) + C$, $S_\mathrm{a} = \left|\frac{\mathrm{dFIR}}{\mathrm{d}T}\right| = \left|A \times \exp\left(-\frac{T}{B}\right) \times \frac{1}{B}\right|$ and $S_\mathrm{r} = \left|\frac{\mathrm{dFIR}}{\mathrm{d}T} \times \frac{1}{\mathrm{FIR}}\right| \times 100\%$, where A, B, and C are the fitting parameters and T is the absolute temperature (K).[57] As shown in Fig. S18–S20 (ESI†), the emission at 850 nm has a higher temperature sensitivity than that at 650 nm, suggesting that the process of the transition from high-energy triplet states to low-energy triplet states is influenced by non-radiative transition processes.

Photothermal conversion and solar evaporation

Optical data reveal that **1*** tends to possess excellent photothermal conversion performance at room temperature. Before irradiation, the temperature of **1** did not show a significant increase under the laser irradiation of 1 W $\mathrm{cm^{-2}}$ at 808 nm. However, **1*** warmed up to 185 °C within 1 minute (Fig. 4a), and the structure remained stable under laser irradiation (Fig. S21, ESI†). Five heating–cooling cycles of **1*** demonstrated that the photothermal conversion properties remained highly stable (Fig. 4b), while the power-dependent photothermal conversion tests indicated that the temperature (ΔT) increased along with the increase of power density (Fig. 4c). The linear relationship between ΔT and power density also verified that the excellent photothermal conversion performance had good controllability and operability (Fig. S22, ESI†). The dynamic IR thermal images of **1*** confirmed the rapid accumulation of heat, and the heat could be dissipated rapidly within 40 seconds after the removal of the 808 nm laser (Fig. 4d). This phenomenon verifies that **1*** has a swift response rate of the photothermal conversion effect, confirming that it is an outstanding controllable material. The photothermal conversion effect of **1*** can be well-described by the linearly fitted time constant τ_s of 784.2 seconds (Fig. 4e) and the competitive efficiency of 45.09% (the specific calculation process is shown in the ESI†).

According to EPR data, the photoinduced radicals of **1*** remain stable in water. Hence, solar-driven water evaporation experiments were carried out on the **1***-loaded airlaid paper covering water to assess the practical application of the photothermal conversion (Fig. S23, ESI†). When sample **1*** was immersed directly in water and tested under 808 nm laser irradiation, the temperature of the **1*** suspension increases to around 30 °C, while the temperature of pure water is 23 °C (Fig. 4f). This phenomenon implies that the sample will bring about excellent solar-driven water evaporation properties. Furthermore, sample **1*** was loaded on airlaid paper and then covered with water to perform standard water evaporation efficiency characteration. Under AM 1.5 G irradiation, the temperature of the pristine airlaid paper increased by 8 °C, while the temperature of the **1***-loaded airlaid paper rapidly increased by 17 °C (Fig. 4g). The heat trapped in the sample and escaped into the environment, promoting evaporation and reducing the mass of the water. When irradiated for 30 minutes, the water evaporation effect brought by sample **1*** led to a mass loss of 0.6 kg $\mathrm{m^{-2}}$, while the blank airlaid paper showed a mass reduction of 0.3 kg $\mathrm{m^{-2}}$ (Fig. 4h). Five parallel cycles confirmed the stability of water evaporation performance and yielded an average evaporation rate of 1.232 kg $\mathrm{m^{-2}\ h^{-1}}$ (Fig. 4i). A high solar-driven water evaporation efficiency of 80.0% is presented, which reveals that the appearance of the ultrahard photoinduced radicals results in outstanding water evaporation photothermal conversion performance.

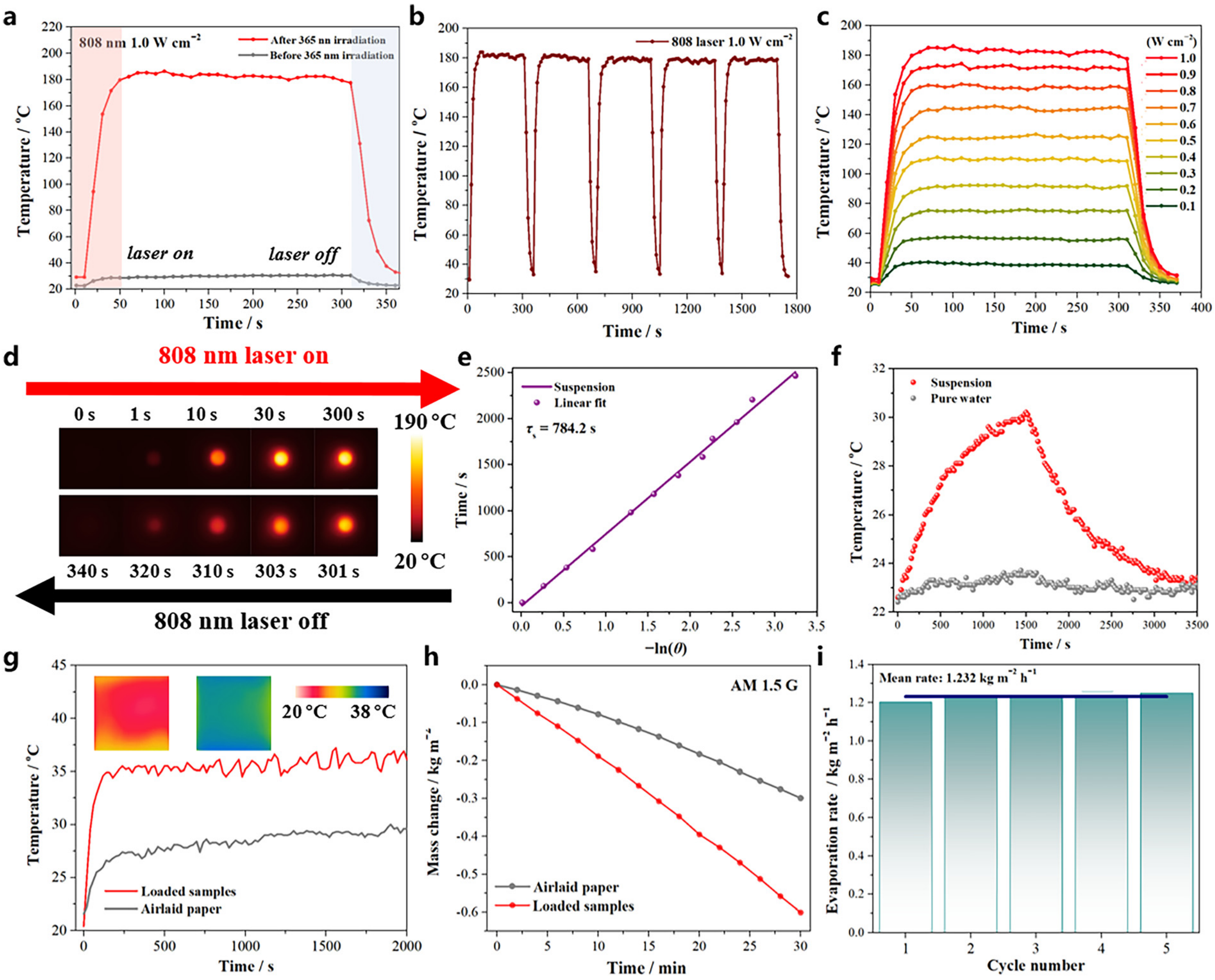

Fig. 4 (a) Photothermal conversion curves of **1** (grey line) and **1*** (red line) under 1 W cm^{-2} 808 nm laser irradiation. (b) Five heating–cooling cycles for photoproduct **1***. (c) Photothermal conversion curves of irradiated **1*** at different NIR laser intensities. (d) IR thermal images of **1*** under on and off irradiation of the 1 W cm^{-2} 808 nm laser. (e) Plot of time *versus* −ln(θ) according to the data recorded using an IR camera during the cooling period. (f) Photothermal conversion curves of **1*** suspension in water (red circles). The properties of pure water are also provided as a comparison (grey circles). (g) Temperature changes of pristine airlaid paper (grey line) and photoproduct **1*** loaded on airlaid paper (red line) taking up water under AM 1.5G irradiation. The inset shows the photographs captured using an IR thermal camera upon 1 sunlight. (h) Water evaporation curves with airlaid paper (grey line) and **1***-loaded airlaid paper (red line) under AM 1.5G. (i) The solar-driven water evaporation rate of **1***-loaded airlaid paper in five cycles, with a mean rate of 1.232 kg m^{-2} h^{-1}.

Theoretical calculation and analysis

To gain further insights into the origin of photoinduced radicals, DFT/TD-DFT calculations were carried out to assess the singlet state of **1** and the triplet state of **1***. For the singlet state, the highest occupied molecular orbital (HOMO, Fig. 5a) and the lowest unoccupied molecular orbital (LUMO, Fig. 5b) are mainly delocalized to pyridine and ethylene units, respectively, with the HOMO–LUMO gap of 4.27 eV. For the simulated UV-Vis-NIR absorption spectrum, there is a single broad peak with the strongest oscillator strength located at 323.85 nm (Fig. 5c). As can be observed from the visualization, the transition originates mainly from the pyridine (HOMO−6) to the ethylene group (LUMO+2). Considering the other sub-strong oscillator positions, such as 328.89, 324.68 and 314.60 nm, the absorption transitions are mostly similar to that at 323.85 nm (Fig. S24–S26, ESI†).

In contrast, the excited state of **1*** possesses more abundant properties. The spin density distribution of **1*** reveals that the spin density is mainly delocalized on the central ethylene unit, suggesting that it is the active site of the photoinduced electron transfer process (Fig. S27, ESI†). An in-depth examination of the energy of the frontier molecular orbitals shows that the HOMO and the LUMO have energy levels of −5.71 eV and −4.26 eV, respectively (Fig. 5d and e), and the electron clouds of both are primarily distributed in pyridine units. To study the changes of absorption in the UV, visible and NIR regions of **1***, the simulated absorption spectra of three optical regions are analyzed in detail. The transition at 314.60 nm is similar to the singlet state (Fig. S28, ESI†), while the variation at 324.94 nm clearly shows that the electron cloud changes in the ethylene bond (Fig. S29, ESI†). Based on the experimental data, the absorbance of **1** at 276 and 294 nm decreased with the increase of illumination time, which indicates the generation of ethylene radicals.

The increase in absorption in the visible region suggests the secondary processes of ethylene radicals. Transitions at 483.26 nm

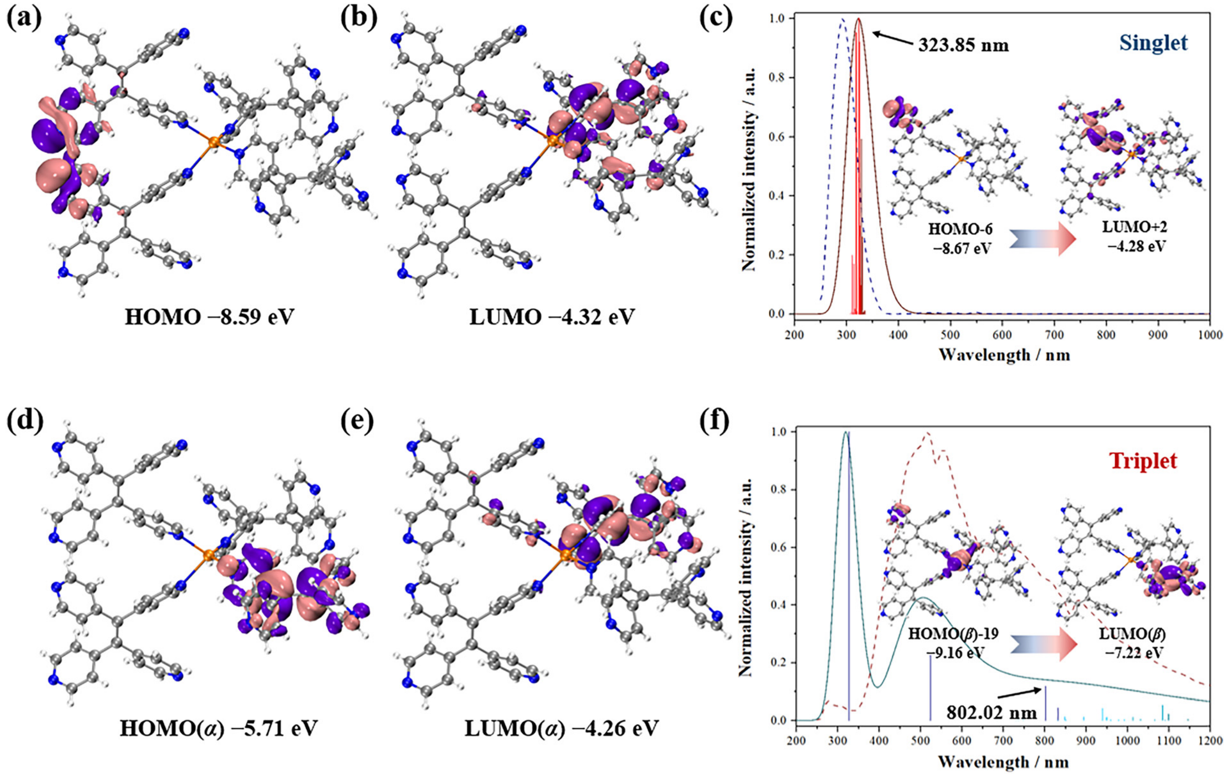

Fig. 5 Energy diagrams optimized by the B3LYP function and def2-svp basis sets, as well as pictorial representations of the HOMO (a) and LUMO (b) of **1** (with ADC$^-$ anionic guests omitted) in the singlet state. (c) Experimental (dashed blue line) and simulated (solid red line) UV-Vis-NIR absorption spectra of **1** in the singlet state based on TD-DFT calculations. The strongest oscillator strength at 323.85 nm was derived from the transition from HOMO−6 to LUMO+2. For the triplet state, the frontier molecular orbitals ((d) for the LUMO and (e) for the HOMO) and the simulated UV-Vis-NIR absorption spectrum ((f), solid blue line) of **1*** are shown, with the experimental data (dashed red line) for comparison. The visualization was conducive to discussing the absorption at 802.02 nm, indicating the transition from HOMO−19 to the LUMO. The vertical solid red/blue lines indicate the oscillator strengths of the simulated absorption peaks. Color code: Ag, orange; C, silver; N, blue; and H, white.

and 523.07 nm hint that the electron cloud will delocalize to the adjacent pyridine ring (Fig. S30 and S31, ESI†), while absorption at 571.88 nm indicates that electrons located in pyridine will resonate on the ethylene bond again (Fig. S32, ESI†). The reversible resonance process of the diradical is reasonable,[58] which confirms the deduction that the conjugated groups can stabilize ethylene radicals. Interestingly, the theoretical absorption mechanism in the NIR region is different from that in the UV and visible regions. As can be seen from Fig. 5f, the HOMO−19 has the participation of the $4d_{z^2}$ orbital of Ag, while the electron cloud of the LUMO is distributed around the ethylene group, which exhibits the inter-ligand transitions that are different from those described above.[59,60] Therefore, despite utilizing the non-conjugated ADC$^-$ guests, **1*** can still show ultra-stable properties and excellent photothermal conversion properties, which may be related to the potential metal to ligand charge transfer process.

Conclusions

Herein, we have synthesized crystalline material MOF **1** through the self-assembly of the large steric-hindered non-conjugated anionic guests and the cationic silver framework. Under irradiation at 365 nm, **1** can be transformed into EPR-active photochromic product **1***. The time-dependent UV-Vis-NIR diffuse reflectance spectra demonstrate that the three light regions in the generation process of **1*** have significantly different dynamic changes. Particularly, the absorption in the NIR region rapidly increases along with the accumulation of irradiation time. The photochromic behavior follows the photoinduced-radical mechanism, and the **1*** radical possesses ultrahigh water and air stability. The variable-temperature EPR spectra show that **1*** has a rare thermal enhancement property, which is attributed to the appearance of the thermal excitation triplet state. The photoluminescence spectra also provide spectroscopic evidence for the generation of thermally excited triplets, showing not only the broadband red/NIR emission of the radicals but also the room temperature phosphorescence behavior at the millisecond level. Interestingly, in spite of the excellent emission behavior, **1*** still exhibits a competitive photothermal conversion behavior. Under the irradiation of an 808 nm laser, the measured photothermal conversion efficiency is 45.09%. At the same time, the evaporation rate of the solar-driven water evaporator can reach 80% under 1 kW m^{-2} solar irradiation, and the evaporation rate can reach 1.232 kg m^{-2} h^{-1}. In this work, silver MOFs with a thermally excited triplet state were designed and synthesized by utilizing photoinduced radicals, and excellent photothermal conversion performance for solar-driven water evaporation was achieved while ensuring a long decay lifetime at the phosphorescence scale.

Conflicts of interest

There are no conflicts to declare.

Data availability

The data supporting this article have been included as part of the ESI.† The crystallography data have been deposited at the Cambridge Crystallographic Data Centre (CCDC). CCDC 2415265 contains the supplementary crystallographic data for this paper.†

Acknowledgements

This work was supported by the National Natural Science Foundation of China (No. 22488101 and 22131011). The authors wish to acknowledge the Inorganic and Elemental Analysis Platform of the Instrumental Analysis & Research Center of Sun Yat-Sen University for the help with photoluminescence measurements and analyses.

Notes and references

1 S. Gorgon, K. Lv, J. Grüne, B. H. Drummond, W. K. Myers, G. Londi, G. Ricci, D. Valverde, C. Tonnelé, P. Murto, A. S. Romanov, D. Casanova, V. Dyakonov, A. Sperlich, D. Beljonne, Y. Olivier, F. Li, R. H. Friend and E. W. Evans, *Nature*, 2023, **620**, 538–544.

2 Q. Peng, M. U. Hwang, Á. Rentería-Gómez, P. Mukherjee, R. M. Young, Y. Qiu, M. R. Wasielewski, O. Gutierrez and K. A. Scheidt, *Science*, 2024, **385**, 1471–1477.

3 M. Abe, *Chem. Rev.*, 2013, **113**, 7011–7088.

4 C. A. Gould, J. Marbey, V. Vieru, D. A. Marchiori, R. David Britt, L. F. Chibotaru, S. Hill and J. R. Long, *Nat. Chem.*, 2021, **13**, 1001–1005.

5 Y. Pang, N. Nöthling, M. Leutzsch, L. Kang, E. Bill, M. van Gastel, E. Reijerse, R. Goddard, L. Wagner, D. SantaLucia, S. DeBeer, F. Neese and J. Cornella, *Science*, 2023, **380**, 1043–1048.

6 T. S. Cameron, A. Decken, R. M. Kowalczyk, E. J. L. McInnes, J. Passmore, J. M. Rawson, K. V. Shuvaev and L. K. Thompson, *Chem. Commun.*, 2006, 2277–2279.

7 T. Stuyver, B. Chen, T. Zeng, P. Geerlings, F. De Proft and R. Hoffmann, *Chem. Rev.*, 2019, **119**, 11291–11351.

8 P.-Z. Wang and J.-R. Chen, *Nat. Chem.*, 2023, **15**, 1058–1059.

9 S. Biswas, R. Trevino, S. O. Fremin, L. M. Sanchez-Palestino, B. R. Dhungana, A. Porey, W. B. Hughes, H. D. Arman, O. V. Larionov and M. P. Doyle, *J. Am. Chem. Soc.*, 2025, **147**, 12308–12317.

10 M. L. Kirk, D. A. Shultz, A. R. Marri, P. Hewitt and A. van der Est, *J. Am. Chem. Soc.*, 2022, **144**, 21005–21009.

11 L. Ma, J. Chang, Q. Chen, T. Zou, W. Wu and H. Wang, *NPG Asia Mater.*, 2022, **14**, 45.

12 Y. Zhao, Y. Zhang, T. Wang, R. Pei, Y. Zhao, X. Xue and X. Wang, *Angew. Chem., Int. Ed.*, 2024, **63**, e202411180.

13 Q. Jiang, H. Wei, X. Hou and C. Chi, *Angew. Chem., Int. Ed.*, 2023, **62**, e202312538.

14 T. Jousselin-Oba, M. Mamada, J. Marrot, A. Maignan, C. Adachi, A. Yassar and M. Frigoli, *J. Am. Chem. Soc.*, 2019, **141**, 9373–9381.

15 C. Chen, Y. Zhang, X.-Y. Wang, J.-Y. Wang and J. Pei, *Chem. Mater.*, 2023, **35**, 10277–10294.

16 L. Wang, H. Wang, S. Yu, N. An, Y. Pan, J. Li, T. Jia, K. Wang and W. Huang, *Adv. Funct. Mater.*, 2024, **34**, 2315762.

17 J. Huang, Z. Wang, W. Zhu and Y. Li, *Aggregate*, 2024, **5**, e426.

18 K. K. Hollister, A. Molino, N. Jones, V. V. Le, D. A. Dickie, D. S. Cafiso, D. J. D. Wilson and R. J. Gilliard, *J. Am. Chem. Soc.*, 2024, **146**, 6506–6515.

19 Q. Wei, J. Huang, Q. Meng, Z. Zhang, S. Gu and Y. Li, *Adv. Sci.*, 2024, **11**, 2406800.

20 X. Hu, H. Chen, L. Zhao, M. Miao and Y. Zheng, *Chem. Mater.*, 2019, **31**, 10256–10262.

21 B. Yang, S. Yan, S. Ban, Y. Zhang, H. Ma and W. Huang, *Chem. Mater.*, 2024, **36**, 7940–7952.

22 D. Li, X. Chen, W. Dai, Q. Jin, D. Wang, J. Ji and B. Z. Tang, *Coord. Chem. Rev.*, 2019, **378**, 365–381.

23 M. Sacherer and H. Dube, *Adv. Mater.*, 2025, **37**, 2411223.

24 G. C. Thaggard, B. K. P. M. Kankanamalage, K. C. Park, J. Lim, M. A. Quetel, M. Naik and N. B. Shustova, *Adv. Mater.*, 2024, 2410067.

25 J. Haimerl, G. C. Thaggard, B. K. P. Maldeni Kankanamalage, R. Bühler, J. Lim, K. C. Park, J. Warnan, R. A. Fischer and N. B. Shustova, *J. Am. Chem. Soc.*, 2025, **147**, 19918–19930.

26 X.-Q. Wang, Y.-W. Geng, Z. Wang, C. Xie, T. Han and P. Cheng, *J. Am. Chem. Soc.*, 2025, **147**, 18044–18053.

27 P.-Y. Liao, Y. Liu, Z.-Y. Ruan, H.-L. Wang, C.-G. Shi, W. Deng, S.-G. Wu, J.-H. Jia and M.-L. Tong, *Inorg. Chem.*, 2023, **62**, 1075–1085.

28 P.-Y. Liao, J.-X. Li, J.-C. Liu, Q. Xiong, Z.-Y. Ruan, T. Li, W. Deng, S.-D. Jiang, J.-H. Jia and M.-L. Tong, *Angew. Chem., Int. Ed.*, 2024, **63**, e202401448.

29 P.-Y. Liao, H.-R. Xing, Y.-L. Zhong, X.-N. Xu, P.-X. Lu, S.-D. Jiang, C.-H. Li, J.-L. Liu, R. A. Layfield and M.-L. Tong, *J. Am. Chem. Soc.*, 2025, **147**, 22714–22724.

30 W.-J. Wei, Y. Mu, L. Wei, J.-X. Hu and G.-M. Wang, *Inorg. Chem.*, 2021, **60**, 108–114.

31 H. Xie, J. Wang, Z. Lou, L. Hu, S. Segawa, X. Kang, W. Wu, Z. Luo, R. T. K. Kwok, J. W. Y. Lam, J. Zhang and B. Z. Tang, *J. Am. Chem. Soc.*, 2024, **146**, 18350–18359.

32 J. Wang, Y. Li, L. Deng, N. Wei, Y. Weng, S. Dong, D. Qi, J. Qiu, X. Chen and T. Wu, *Adv. Mater.*, 2017, **29**, 1603730.

33 X. Chen, N. Yang, Y. Wang, H. He, J. Wang, J. Wan, H. Jiang, B. Xu, L. Wang, R. Yu, L. Tong, L. Gu, Q. Xiong, C. Chen, S. Zhang and D. Wang, *Adv. Mater.*, 2022, **34**, 2108048.

34 D. Xi, M. Xiao, J. Cao, L. Zhao, N. Xu, S. Long, J. Fan, K. Shao, W. Sun, X. Yan and X. Peng, *Adv. Mater.*, 2020, **32**, 1907855.

35 J. Sun, E. Zhao, J. Liang, H. Li, S. Zhao, G. Wang, X. Gu and B. Z. Tang, *Adv. Mater.*, 2022, **34**, 2108048.

36 Z. Wang, J. Zhou, Y. Zhang, W. Zhu and Y. Li, *Angew. Chem., Int. Ed.*, 2022, **61**, e202113653.

37 L. Yang, G. Wang, Y. Zhang, J. Zhou, R. Wu, C. Qin, Q. Chang, C. Zhang, S. Duan and X. Gu, *Angew. Chem., Int. Ed.*, 2025, e202508821.

38 Y.-L. Gao, L.-X. Zhao, Q.-Y. Du, L.-L. Guo, H.-X. Sun, S.-Z. Li, H.-W. Cui, X.-Y. Geng, X.-Y. Li and G.-M. Wang, *Inorg. Chem.*, 2025, **64**, 8001–8008.

39 S. Kusumoto, T. Mio, K. Rakumitsu, M. Shimabukuro, M. Kobayashi, T. Fukui, N. Hamamoto, T. Ishizaki, Y. Kim and Y. Koide, *J. Mater. Chem. C*, 2025, **13**, 3408–3413.

40 K. Xu, B. Yu, Y. Li, H. Su, B. Wang, K. Sun, Y. Liu, Q. Peng, H. Hou and K. Li, *Chem. Commun.*, 2018, **54**, 12942–12945.

41 M. Peng, Y. Luo, Y. Rao, J. Song and X. Ni, *Chem. Eur. J.*, 2022, **28**, e202202056.

42 S. Yan, B. Yang, F. Feng, Y. Zhang, S. Ban, H. Ma and W. Huang, *Sci. China:Chem.*, 2024, **68**, 661–669.

43 S. Park, J. Lee, H. Jeong, S. Bae, J. Kang, D. Moon and J. Park, *Chem*, 2022, **8**, 1993–2010.

44 L. Liu, Q. Liu, R. Li, M.-S. Wang and G.-C. Guo, *J. Am. Chem. Soc.*, 2021, **143**, 2232–2238.

45 T. Xu, Y. Han, Z. Shen, X. Hou, Q. Jiang, W. Zeng, P. W. Ng and C. Chi, *J. Am. Chem. Soc.*, 2021, **143**, 20562–20568.

46 Q. Dang, L. Hu, L. Yuan, X. Miao, A. Huang, J. Su, J. Wang, Y. Zhou, X. Chen, Q. Li, Z. Li and X. Deng, *Angew. Chem., Int. Ed.*, 2023, **62**, e202312538.

47 S. Mori, M. Akita, S. Suzuki, M. S. Asano, M. Murata, T. Akiyama, T. Matsumoto, C. Kitamura and S. Kato, *Chem. Commun.*, 2020, **56**, 5881–5884.

48 A. Maiti, F. Zhang, I. Krummenacher, M. Bhattacharyya, S. Mehta, M. Moos, C. Lambert, B. Engels, A. Mondal, H. Braunschweig, P. Ravat and A. Jana, *J. Am. Chem. Soc.*, 2021, **143**, 3687–3692.

49 T. Li, J.-C. Liu, E.-P. Liu, B.-T. Liu, J.-Y. Wang, P.-Y. Liao, J.-H. Jia, Y. Feng and M.-L. Tong, *Chem. Sci.*, 2024, **15**, 1692–1699.

50 J.-C. Liu, T. Li, H. Yu, J. Y. Huang, P. Li, Z.-Y. Ruan, P.-Y. Liao, C. Ou, Y. Feng and M.-L. Tong, *Angew. Chem., Int. Ed.*, 2024, **64**, e202413805.

51 Z. Zhang, Z. Xiong, J. Zhang, B. Chu, X. Liu, W. Tu, L. Wang, J. Z. Sun, C. Zhang, H. Zhang, X. Zhang and B. Z. Tang, *Angew. Chem., Int. Ed.*, 2024, **63**, e202403827.

52 J. Jin, H. Jiang, Q. Yang, L. Tang, Y. Tao, Y. Li, R. Chen, C. Zheng, Q. Fan, K. Y. Zhang, Q. Zhao and W. Huang, *Nat. Commun.*, 2020, **11**, 842.

53 B. Yang, S. Yan, Y. Zhang, S. Ban, H. Ma, F. Feng and W. Huang, *J. Am. Chem. Soc.*, 2024, **146**, 7668–7678.

54 X. Wang, C. Chen, Y. Tian and Q.-W. Zhang, *J. Am. Chem. Soc.*, 2025, **147**, 17994–18002.

55 C. H. Mak, Y. Ai, C. Tan, W. Niu, K.-C. Cheng, C.-W. Hsieh, H.-H. Shen, Z. Hu, Y. Tian, X. Xu, G. Zou, D.-J. Lee and H.-Y. Hsu, *J. Mater. Chem. C*, 2025, **13**, 8671–8681.

56 A. Abdurahman, J. Wang, Y. Zhao, P. Li, L. Shen and Q. Peng, *Angew. Chem., Int. Ed.*, 2023, **62**, e202300772.

57 R. Li, X. Wu, Y. Chen, Q. Zeng, T. Deng and T. Yu, *ACS Appl. Nano Mater.*, 2024, **7**, 15288–15297.

58 Z. Li, X. Liu, Q. Bao, J. Wang, X. Liu, H. Gong, T. Han, C. Feng, D. Lu, L. Yue, C. Wu, G. He, Y. Su and B. Rao, *J. Am. Chem. Soc.*, 2025, **147**, 1452.

59 Y. Ding, P. Liao, J. Jia and M. Tong, *Chin. J. Inorg. Chem.*, 2025, **41**, 141–148.

60 J.-C. Liu, T. Li, P.-Y. Liao, Z.-Y. Ruan, Z.-H. Wang, J.-H. Jia and M.-L. Tong, *Sci. China: Chem.*, 2025, DOI: 10.1007/s11426-025-2608-4.